www.acsnano.org

Magnetic Order, Electrical Doping, and Charge-State Coupling at Amphoteric Defect Sites in Mn-Doped 2D Semiconductors

Akash Singh, Christopher C. Price, and Vivek B. Shenoy*



Downloaded via UNIV OF PENNSYLVANIA on May 22, 2023 at 18:02:06 (UTC). See https://pubs.acs.org/sharingguidelines for options on how to legitimately share published articles.

Cite This: ACS Nano 2022, 16, 9452-9460



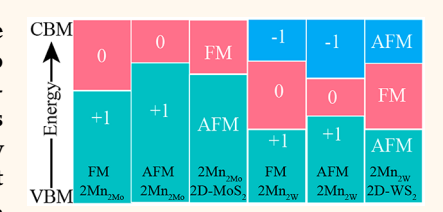
ACCESS

Metrics & More

Article Recommendations

s Supporting Information

ABSTRACT: Two-dimensional (2D) dilute magnetic semiconductors (DMSs) are attractive material platforms for applications in multifunctional nanospintronics due to the prospect of embedding controllable magnetic order within nanoscale semiconductors. Identifying candidate host material and dopant systems requires consideration of doping formation energies, magnetic ordering, and the tendency for dopants to form clustered domains. In this work, we consider the defect thermodynamics and the dilute magnetic properties across charge states of 2D-MoS₂ and 2D-WS₂ with Mn magnetic dopants as candidate systems for 2D-DMSs. Using



hybrid density functional calculations, we study the magnetic and electronic properties of these systems across configurations with thermodynamically favorable defects: $2D\text{-MoS}_2$ doped with Mn atoms at sulfur site (Mn_S), at two Mo sites ($2Mn_{Mo}$), on top of a Mo atom (Mn-top), and at a Mo site ($4Mn_{Mo}$). While the majority of the Mn-defect complexes provide trap states, Mn_{Mo} and Mn_W are amphoteric, although previously predicted to be donor defects. The impact of cluster formation of these amphoteric defects on magnetic ordering is also considered; both Mn_{Mo}-Mn_{Mo} ($2Mn_{2Mo}$) and Mn_W-Mn_W ($2Mn_{2W}$) clusters are found to be stable in ferromagnetic (FM) ordering. Interestingly, we observed the defect charge state dependent magnetic behavior of $2Mn_{2Mo}$ and $2Mn_{2W}$ clusters in 2D-TMDs. We investigate that the FM coupling of $2Mn_{2Mo}$ and $2Mn_{2W}$ clusters is stable in only a neutral charge state; however, the antiferromagnetic (AFM) coupling is stable in the +1 charge state. $2Mn_{2Mo}$ clusters provide shallow donor levels in AFM coupling and deep donor levels in FM coupling. $2Mn_{2W}$ clusters lead to trap states in the FM and AFM coupling. We demonstrate the AFM to FM phase transition at a critical electron density $n^{c}_{e} = 3.5 \times 10^{13}$ cm⁻² in 2D-MoS₂ and 2D-WS₂. At a 1.85% concentration of Mn, we calculate the Curie temperature of 580 K in the mean-field approximation.

KEYWORDS: 2D-MoS₂, 2D-WS₂, defects, charge state, ferromagnetic, antiferromagnetic

INTRODUCTION

Dilute magnetic semiconductors (DMSs) have attracted much attention because of their potential nanoscale magnetic and electronic applications. $^{1-10}$ A fundamental challenge in nanoscale spin-based electronics or spintronics is finding two-dimensional (2D) magnetic materials with both high Curie temperature ($T_{\rm c}$) and large spin polarization, which offer opportunities for the next-generation information technology via faster device operation and high information storage density. $^{11-18}$ Recently, 2D-CrI $_{\rm 3}^{13}$ and 2D-Cr $_{\rm 2}$ Ge $_{\rm 2}$ Te $_{\rm 6}^{14}$ have shown promise for low-temperature 2D spintronics. However, the $T_{\rm c}$ of these materials is far below the liquid-nitrogen temperature (77 K) and hence restricts their applications. Therefore, developing 2D magnetic materials possessing robust long-range spin ordering and high $T_{\rm c}$ is a significant outstanding challenge in materials design.

Within all the 2D materials, the transition metal dichalcogenides (TMDs) family, including MoS₂ and WS₂ nanosheets, has been heavily studied for a variety of

nanoelectronic and nano-optoelectronic applications. ^{19–29} Pristine monolayer TMDs are nonmagnetic semiconductors, and the artificial manipulation of the valence d orbitals can induce magnetism, half-metallicity, and electrical control of spin polarization. ^{22,23,25,30–32} To obtain stable magnetism in 2D-TMDs at room temperature and beyond, various methods have been proposed, and among these, magnetic doping has proven to be a successful strategy. ^{33–38} Due to the many structural and electronic degrees of freedom present at doping concentrations high enough to observe magnetic ordering, the

Received: March 9, 2022 Accepted: May 24, 2022 Published: May 26, 2022





relationship between atomic doping, electronic doping, and magnetic ordering remains underexplored.

Previous studies have shown that isolated Mn doping at the Mo site (i.e., Mn_{Mo}) in 2D-MoS₂ promotes magnetism, ^{39–41} but experimentally these isolated defects have been observed to cluster together. Apart from isolated Mn_{Mo}, Mn_{Mo}-Mn_{Mo} (i.e., 2Mn_{2Mo}) cluster formation is observed in 2D-MoS₂, and these clusters appear more than the well-dispersed single Mn_{Mo}. 42 Moreover, other experimental reports 43 suggest the presence of many other Mn-defect complexes such as a Mn atom at sulfur site (Mn_S), a Mn atom on top of Mo (Mn-top), and a Mn atom at a Mo site (Mn_{Mo}). The role of these alternative dopant-defect structures on the magnetic and electronic properties of 2D-TMDs has not yet been considered. Furthermore, in previous studies of isolated Mn_{Mo}, the defect charge state for 3d impurities was not considered, and this is both highly sensitive to the Fermi-level position of the host material and critically important for magnetic ordering. 44-46 The charge state can be controlled by manipulating the Fermi level through free-carrier doping 47-49 via other structural defects, doping by suitable electron donors and acceptors in 2D-TMDs, or electrostatic gating. 50,51 Therefore, we study the thermodynamics of defect formation and the effect of charge state on the magnetic ordering across experimentally observed Mn defects and their complexes in 2D-MoS₂ and 2D-WS₂.

Apart from a high T_o , a large magnetic anisotropy energy (MAE), *i.e.*, the energy barrier favoring a particular spatial orientation of the magnetic moments, is a desirable quantity for an ideal dilute magnetic semiconductor.^{39,40} Magnetic doping, such as a Mn atom at a Mo site in 2D-MoS₂ or at a W site in 2D-WS₂, leads to a redistribution of local orbital energies due to the crystal field effect; the dopant orbital magnetic moment distribution and the associated MAE are determined by the crystal field effect.

In this work, all the calculations have been performed using hybrid density functional theory. We have carried out a comprehensive study of magnetic and electronic properties of experimentally observed Mn defects and complexes such as a Mn atom at a sulfur site (i.e., Mn_S), two Mn atoms at a Mo site (i.e., 2Mn_{Mo}), a Mn atom on top of a Mo atom (Mn-top), a Mn atom at a Mo site (Mn_{Mo}) in 2D-MoS₂, and a Mn atom at a W site (Mn_W) in 2D-WS₂. Most of them provide deep levels and free electron/hole trapping centers. Interestingly, Mn_{Mo} is stable as both a donor and an acceptor defect within the band gap, which was previously predicted to be an only donor defect. Mn_S and 2Mn_{Mo} are stable as an electrically neutral and a negative-U defect, respectively. To simulate the effect of clustering, we consider two Mn dopant atoms at neighboring sites, calculate the formation energy, and compare it to the isolated defects. The defect clusters we considered are $\mathrm{Mn}_{\mathrm{Mo}} Mn_{Mo}$ (i.e., $2Mn_{2Mo}$) and Mn_W-Mn_W (i.e., $2Mn_{2W}$) in 2D-MoS₂ and 2D-WS₂, respectively, and found that they are stable in ferromagnetic (FM) and antiferromagnetic (AFM) coupling in the neutral and +1 charge state, respectively. Unlike isolated Mn_{Mo}, the clustered 2Mn_{2Mo} provides a shallow donor level in the AFM coupling. Although most of the doping properties in WS₂ are similar to those in MoS₂, the 2Mn_{2W} cluster instead provides deep levels in both FM and AFM coupling. We demonstrate the AFM to FM phase transition at a critical electron density $n_e^c = 3.5 \times 10^{13} \text{ cm}^{-2}$, in the n-doped 2D-MoS₂ and 2D-WS₂. Finally, for a reasonable Mn doping concentration of 1.85%, we calculated a Curie temperature of 580 K using the mean-field approximation.

RESULTS AND DISCUSSION

Pristine 2D-MoS₂ and 2D-WS₂ have hexagonal crystal structures, where metal atoms sandwiched between two layers of chalcogen atoms form chalcogen—metal—chalcogen bonds in the unit cell.^{25,26} The calculated lattice parameters of 2D-MoS₂ and 2D-WS₂ are essentially identical and found to be 3.18 Å, agreeing with previous reports.²⁵ The bond length of Mo–S (W–S) is 2.42 Å (2.41 Å), and the distance of two S atomic planes is 3.14 Å (3.13 Å). The HSE06-calculated direct band gaps of 2D-MoS₂ and 2D-WS₂ are 1.9 and 2.1 eV, respectively, at the K-point, agreeing well with previous reports.^{52,53} The optimized geometries of all the considered Mn defects are shown in Figure 1. The top views are shown in

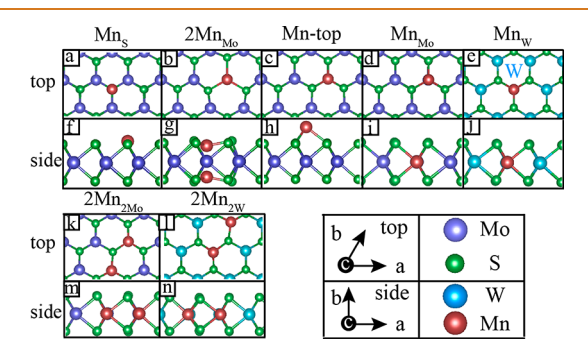


Figure 1. Top view of the fully optimized crystal structure of (a) Mn substituting a sulfur atom (Mn_S), (b) two Mn atoms at the Mo site (2Mn_{Mo}), (c) Mn on top of a Mo atom (Mn-top), (d) Mn substituting a Mo atom (Mn_{Mo}) in 2D-MoS₂, and (e) Mn substituting a W atom (Mn_W) in 2D-WS₂. Panels (f) to (j) represent their respective side view. Top view of the fully optimized crystal structure of (k) the Mn_{Mo}-Mn_{Mo} (2Mn_{2Mo}) cluster in 2D-MoS₂ and (l) the Mn_W-Mn_W (2Mn_{2W}) cluster 2D-WS₂. (m) and (n) give the respective cluster side view.

Figure 1(a to e), and the corresponding side views are shown in Figure 1(f to j). The pristine bond length of Mo-S is 2.41 Å, and after replacing a S with Mn and relaxing the Mn_S defect structure, the substituting bond length of Mn-S is 2.62 Å, as shown in Figure 1(a). In 2Mn_{Mo}, the Mn atoms bind with the three upper and lower S atoms with the Mn-S bond length of 2.18 Å, as shown in Figure 1(b). The optimized distance between Mn and S atoms in Mn-top is found to be 2.40 Å Figure 1(c). Figure 1(d) shows that in Mn_{Mo} six S atoms surrounding the Mn site move inward, and the corresponding Mn-S distance is 2.30 Å. In Mn_W, the corresponding relaxed W-S bond length is 2.31 Å, as shown in Figure 1(e). Next, Figure 1(k and l) represents the optimized geometry of Mn-Mn clustering or pairs, and the relaxed bond lengths of Mn-S and W-S are 2.30 and 2.31 Å, respectively. The atomic radius of Mn (1.38 Å) is very close to that of Mo (1.40 Å) and W (1.41 Å) atoms, so we expected minimal lattice distortion at the metal sites; however, we found that Mn-Mn clustering leads to strong local lattice distortion as the corresponding Mn-Mn distances are 3.29 and 3.44 Å in 2D-MoS₂ and 2D- WS_2 , vs 3.18 and 3.20 Å in the respective pristine cases.

The spin-polarized projected electronic density of states (PDOS) for all isolated Mn defects in 2D-MoS₂ are analyzed and shown in Figure 2. Removing a S atom as in Figure 2(a) provides two excess electrons, which occupy the singlet d_z^2 state near the valence band maxima (VBM) and the two empty doubly degenerate states above the Fermi level (E_F). These defect Kohn–Sham levels originate from Mo- $(d_{xy}, d_x^2 - v^2)$

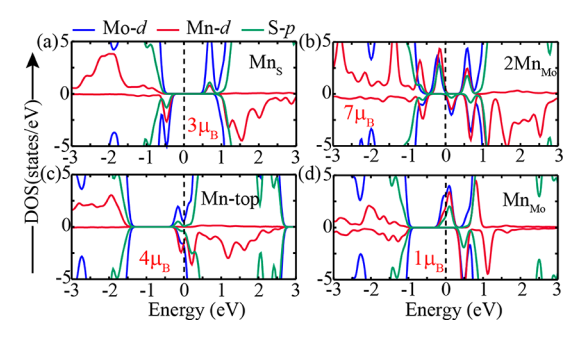


Figure 2. Spin-polarized projected density of states (PDOS) of (a) Mn substituting a sulfur atom (Mn_S), (b) two Mn atoms in the Mo site (2Mn_{Mo}), (c) a Mn atom on top of a Mo atom (Mn-top), and (d) Mn substituting a Mo atom (Mn_{Mo}). The positive and negative y-axis represents the density of spin-up and spin-down states, respectively. The blue, magenta, and green colors represent Mo-d, Mn-d, and S-p orbitals, respectively. Vertical black dashed lines represent the Fermi level.

orbitals. Upon substituting Mn at the S site (Mn_S), the Mn-3d orbitals break the degeneracy of the spin channels and provide a local magnetic moment of 3 $\mu_{\rm B}$, pushing the defect Kohn–Sham levels [Mo(d_{xy}, d_{x²-y²}), Mn(d_{xy}, d_{x²-y²}), Mn(d_{xz}, d_{yz})] near the band edge, as shown in Figure 2(a). The $E_{\rm F}$ is located in the middle of the band gap, and these defect states are present near the band edge; therefore, Mn_S is expected to be stable as an electrically inactive defect. The strong lattice distortion in 2Mn_{Mo} leads to several strongly localized defect states near the $E_{\rm F}$, Figure 2(b). These localized states mainly arise from the Mn-3d, Mo-4d, and S-3p states. A hybridization between Mn-3d, the closest Mo-4d, and S-3p states produces the localized states in the spin-up channel and spin-down channel, providing a local magnetic moment of 7 $\mu_{\rm B}$. 2Mn_{Mo}

leads to half-metallicity in $2D\text{-MoS}_2$ by providing a finite gap in the spin-up and spin-down channel, as shown in Figure 2(b).

In Mn-top, Mn-3d hybridizes with S-3p and Mo-4d states and leads to donor states near the conduction band, making the system metallic, as shown in Figure 2(c). After the hybridization, the Mn-3d antibonding states consisting of d_{xy} and $d_{x^2-y^2}$ orbitals give states in only one spin channel at the E_F , leading to a local magnetic moment of 4 μ_B in 2D-MoS₂; the other spin states are split into the original valence band. In Mn_{Mo}, Mn-3d orbitals strongly hybridize with the S-3p orbitals and provide midgap states, which further split and give the unoccupied antibonding states $Mn(d_{xy}, d_{x^2-y^2})$ and $Mn(d_{xz}, d_{xz})$ d_{vz}) in the spin-down channel and the occupied bonding state $Mn(d_{z^2})$ in the spin-up channel, as shown in Figure 2(d). This occupied spin-up bonding state $Mn(d_z^2)$ provides 1 μ_B magnetic moment per Mn atom. The spin density of Mn_{Mo} is shown in Figure S2 in the Supporting Information. Moreover, we observed no band gap in the spin-up channel and a finite band gap in the spin-down channel, ensuring halfmetallicity when Mn substitutes for Mo in 2D-MoS₂.

For better insight into hybridization between Mo, W, Mn, and S, we analyzed the molecular orbital (MO) picture of 2D-MoS₂ and 2D-WS₂ as shown in Figure 3(a and b). The MO picture is constructed through the irreducible representation for the D_{3h} point group symmetry. The lowest a'₁, e', and e'' are all bonding orbitals, where a'₁ is mostly composed of chalcogen p_x and p_y orbitals and e' and e'' lie on both metal and chalcogen atoms. The a''₂ orbitals which originate through chalcogen p_z orbitals do not hybridize with a metal atom. The highest occupied orbital a'₁ is antibonding (near the Fermi level) and arises through Mo-d [or W-d in Figure 3(b)] orbitals with a small contribution from chalcogen p_x and p_y orbitals. The e' and e'' antibonding orbitals are the first

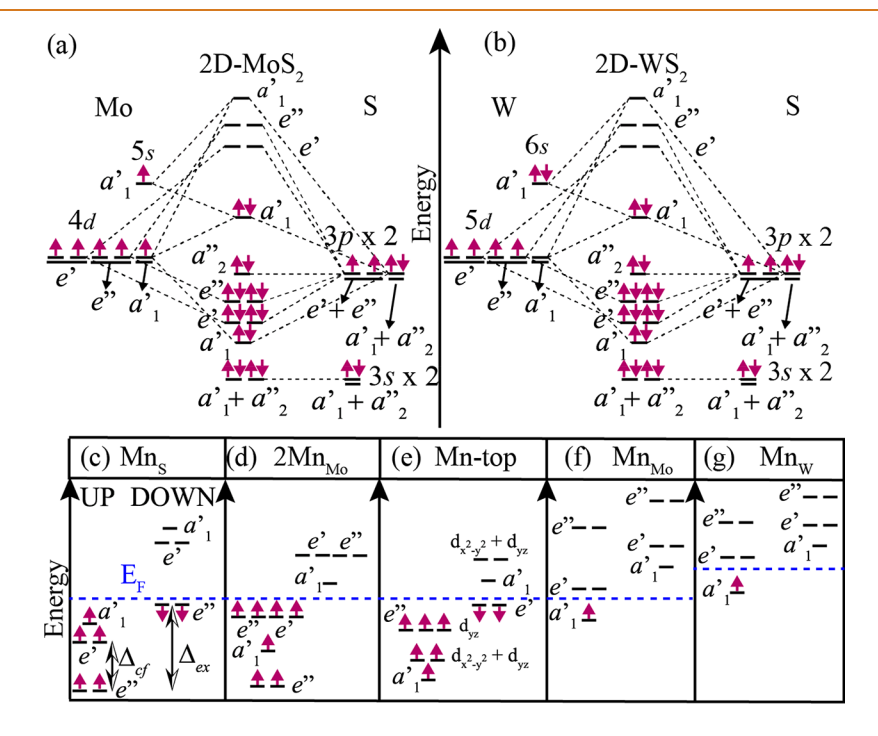


Figure 3. Molecular orbital diagram of (a) 2D-MoS₂ and (b) 2D-WS₂. The types of orbitals are shown in black color with the D_{3h} point group symmetry notation. Black dashed lines represent the symbolic links between the molecular and atomic orbitals. The schematic of crystal-field splitting (Δ_{cf}) and the interatomic Hund's exchange (Δ_{ex}) of the Mn-3d orbitals in (c) Mn_S, (d) 2Mn_{Mo}, (e) Mn-top, (f) Mn_{Mo}, and (g) Mn_W. The horizontal blue dashed line represents the Fermi-level position.

unoccupied orbital sets, and these consist of Mo (or W)-d and S-p orbitals.

Using the band centers method,⁵⁵ we analyzed the crystalfield splitting (Δ_{cf}) and the interatomic Hund's exchange (Δ_{ex}) of Mn-3d orbitals; the schematic is shown in Figure 3(c to g) for the neutral charge-state configurations. A Mn_S defect provides five midgap states, which split into three groups under the trigonal prismatic surroundings of the S atoms, as shown in Figure 3(c). The large overlap of S-3p orbitals with $Mn(d_{xz})$ d_{vz}) makes the antibonding orbital (e") degenerate and raises their energy. The reduced overlapping of the Mn-dz2 antibonding orbital (a'₁) with the S-3p orbitals does not change the energy of the Mn-3d orbitals. Moreover, the moderate overlapping of $Mn(d_{xy}, d_{x^2-y^2})$ antibonding orbitals (e') with S-3p orbitals holds them in between the a'1 and e" orbitals, as shown in the spin-up channel of Figure 3(c). In the case of Mn_S, the exchange splitting of the e orbitals, $\Delta_{ex} = 1.7$ eV, is larger than the crystal field splitting, Δ_{cf} = 400 meV. For $2Mn_{Mo}$, we obtain $\Delta_{ex} = 830$ meV and $\Delta_{cf} = 1.22$ eV. In Mntop, the interaction of chalcogen p orbitals breaks the symmetry, as shown in Figure 3(e). In Mn_{Mo} and Mn_W, Mn substitution leads to occupied Mn-dz2 states just below the conduction band, as shown in Figures 3(f) and (g). For Mn_{Mo} (Mn_W), we find $\Delta_{\rm ex} = 381$ (431) meV and $\Delta_{\rm cf} = 690$ (552) meV.

The formation energy (E^f) of defects provides important information about their stability, concentration and the charge transition levels within the band gap. The E^f of defect [X] in charge state q is given by

$$E^{\text{f}}[X_q] = E^{\text{defect}}_{\text{tot}} - E^{\text{pristine}}_{\text{tot}} - \sum_{i} n_i \mu_i + q E_{_{\text{F}}} + \Delta^q$$

where $E^{\text{defect}}_{\text{tot}}$ and $E^{\text{pristine}}_{\text{tot}}$ are the relaxed energies of the defective and defect-free supercells, respectively. n_i is the number of i-type atoms added $(n_i > 0)$ or removed $(n_i < 0)$ from the pristine supercell. μ_i is the chemical potential of i-type element, referenced to the total energy of a Mo, W, and Mn atom in crystalline bcc phase and a S atom in crystalline orthorhombic α phase. For the stability of 2D-MoS₂, the μ_{Mo} and μ_{S} satisfy the relation of $\mu_{\text{Mo}} + 2\mu_{\text{S}} = \mu_{\text{MoS2}}$, where μ_{MoS2} is the total energy of 2D-MoS₂ per formula unit. In the Mo-rich limit condition, $\mu_{\text{Mo}}^{\text{max}} = E^{\text{tot}}_{\text{Mo}}$, where $E^{\text{tot}}_{\text{Mo}}$ is the total peratom energy of BCC Mo, and the corresponding S-poor condition is given by $\mu_{\text{S}}^{\text{min}} = (\mu_{\text{MoS2}} - \mu_{\text{max}}^{\text{max}})/2$. In the S-rich limit condition; $\mu_{\text{S}}^{\text{max}} = E^{\text{tot}}_{\text{S}}$, in which the $E^{\text{tot}}_{\text{S}}$ is the total peratom energy of the S orthorhombic crystal, where the S orthorhombic crystal is considered to be the reference source of S. The chemical potential conditions of μ_{W} and μ_{S} in 2D-WS₂ are determined analogously to that of μ_{Mo} and μ_{S} in 2D-MoS₂. E_{F} is the Fermi-level position, referenced to VBM. Δ^q represents the charge-state correction due to the finite size of the supercell.

Defect transition levels (DTLs) are the positions of E_F at which the thermodynamically favored charge state of the defect changes from q to q':

$$\varepsilon(q/q') = \frac{E^{f}(X_q) - E^{f}(X_{q'})}{(q'-q)} \left| E_{F=0} \right|$$

where $E^{\rm f}({\rm X}_q)$ and $E^{\rm f}({\rm X}_{q'})$ are the formation energies of a defect $[{\rm X}]$ at the VBM, for charge states q and q', respectively. For $E_{\rm F}$ positions below $\varepsilon(q/q')$, charge state q is stable, and for the $E_{\rm F}$ positions above $\varepsilon(q/q')$, charge state q' is stable.

We calculate E^f as a function of E_F for all the experimentally observed Mn defects in 2D-MoS₂ in the Mo-rich and S-rich condition, as shown in Figure 4(a and b). Only the stable

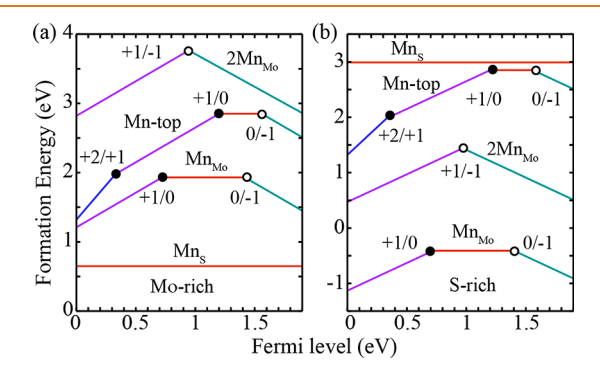


Figure 4. Defect formation energies as a function of the Fermi level of all possible Mn doping in $2D\text{-MoS}_2$ under (a) Mo-rich and (b) S-rich conditions. The Fermi level is referenced to the VBM. Only the most stable charge states are shown, where positive and negative slopes represent the donor and acceptor defects, respectively.

charge states are shown in Figure 4. The E^f values as a function of $E_{\rm F}$ of all these Mn defects in the S(Mo)-rich condition for all the possible charge states are shown in Figure S3 in the Supporting Information. Among all the Mn defects, Mn_S has the lowest E^f , which is 0.65 eV in the Mo-rich condition. However, it has the highest E^{f} (~3 eV) in the S-rich condition compared to other Mn defects in 2D-MoS₂, Figure 4(b). Mn_S is found to be most stable in the neutral charge state (i.e., Mn⁰_S) within the band gap. Therefore, Mn_S is an electrically inactive defect and cannot provide n-type or p-type conductivity to 2D-MoS₂. Moreover, Mn⁰_S induces a local magnetic moment of 3 μ_B , which antiferromagnetically couples with the surrounding Mo atoms and leads to an effective ferromagnetism. The E^{f} of Mn_{Mo}^{0} is 1.93 and -0.41 eV in the Mo-rich and S-rich condition, respectively, Figure 4. Therefore, Mn_{Mo} is more likely to form in the S-rich condition, suggesting a high concentration under typical S-rich synthesis conditions. As a neutral defect, Mn_{Mo} had been previously predicted to be only a donor defect³⁹ by density of states analysis; however, interestingly, we find that Mn_{Mo} is most stable in 0, -1 (an electron acceptor), and +1 (single-electron donor) charge state depending on the $E_{\rm F}$ position, suggesting that this is an amphoteric defect. Mn⁺¹_{Mo} acts as a deep hole trap center (i.e., deep donor defect), and the defect transition level (DTL) $\varepsilon(+1/0)$ of this single donor occurs at 1.19 eV below the conduction band minima (CBM). It can also act as a deep electron trap center with the DTL of $Mn^{\varepsilon(0/-1)}_{Mo}$ at 1.41 eV above the VBM. The thermodynamic analysis suggests that Mn_{Mo} is a charge carrier compensating defect that traps free carriers and inhibits electrical conductivity in 2D-MoS₂. Mn⁰_{Mo} and $\mathrm{Mn}^{-1}_{\mathrm{Mo}}$ induce magnetic moments of 1 μ_{B} and 2 μ_{B} , respectively; conversely, Mn⁺¹_{Mo} is found to be a nonmagnetic defect in 2D-MoS₂.

The E^f of Mn-top⁰ is 2.85 eV in the Mo-rich and S-rich conditions and found to be most stable in +2, +1, 0, and -1 charge state within the E_F range, Figure 4. The DTLs of Mn-top^{ε (+2/+1)} and Mn-top^{ε (+1/0)} occur at 1.59 and 0.7 eV, respectively, below the CBM and ensure a deep donor defect. It is also stable as a deep acceptor defect, and the associated DTL ε (0/-1) is located 1.58 eV above the VBM. Therefore,

although expected to be a shallow donor, we find that Mn-top is both a deep acceptor and deep donor defect. It also induces the magnetic moment of 5 μ_B , 4 μ_B , and 4 μ_B in +2, +1, and 0 charge states, respectively. Figure 4 shows that $2Mn_{\text{Mo}}$ is most stable as a negative-U defect, where +1 and -1 charge states (higher charge state) are more stable than the neutral charge state (lower charge state). The negative-U behavior of $2Mn_{Mo}$ also suggests a strong local lattice distortion, leading to a high formation energy in Mo(S)-rich conditions. The DTL of $2Mn_{Mo}^{\epsilon(+1/-1)}$ occurs 0.93 eV above the VBM (or 0.97 eV below the CBM) and indicates a two-electron transfer phenomenon in the system at that particular value of $E_{\rm F}$. $2Mn_{Mo}$ will pin the Fermi level at $E_F = E_{VBM} + 0.93$ eV, where the $E^{\rm f}$ of $2 {\rm Mn^{+1}}_{\rm Mo}$ and $2 {\rm Mn^{-1}}_{\rm Mo}$ are equal. Therefore, $2 {\rm Mn}_{\rm Mo}$ is always a free charge carrier compensating defect for the entire range of E_F within the gap and reduces the n-type (ptype) conductivity of 2D-MoS₂. Furthermore, 2Mn⁺¹_{Mo} and $2Mn^{-1}_{Mo}$ induce the magnetic moment of 1.3 μ_B and 1 μ_B , respectively. Therefore, our thermodynamic analysis of all Mn defects in 2D-MoS₂ shows that they are generally free charge compensating centers with high formation energies (except for Mn_{Mo} in S-rich conditions and Mn_S in Mo-rich conditions) and inhibit electrical conductivity for 2D-MoS₂. On the other hand, fortunately, all these defects provide local magnetism, and hence their formation is ideal for the application in semiconducting spintronics.

Next, we test the impact of dopant clustering on the magnetic property by comparing the spin-polarized PDOS of $Mn_{Mo}-Mn_{Mo}$ clustering (or $2Mn_{2Mo}$) with the isolated Mn_{Mo} from Figure 2(d), as shown in Figure 5(a, c). In Mn_{Mo} , the

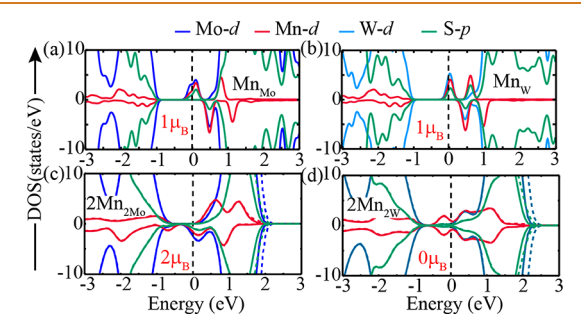


Figure 5. Spin-polarized projected density of states (PDOS) of (a) an isolated Mn atom at the Mo site (Mn_{Mo}) and (b) Mn-Mn clustering $(2Mn_{2Mo})$ in 2D-MoS₂. Spin-polarized PDOS of (c) an isolated Mn atom at the W site (Mn_{W}) and (d) Mn-Mn clustering $(2Mn_{2W})$ in 2D-WS₂. Solid and dashed curves represent the FM and AFM configurations, respectively. The blue, magenta, cyan, and green colors represent the Mo-d, Mn-d, W-d, and S-p orbitals. Vertical red dashed lines represent the Fermi level.

hybridization of Mn-3d and S-4p states provides AFM coupling. On the other hand, when the S spins interact with a Mn_{Mo} defect, the AFM coupling between Mn and S provides an effective ferromagnetic coupling of all the Mn_{Mo} spins. Isolated Mn_{Mo} induces a local magnetic moment of 1 $\mu_{\rm B}$, Figure 5(a). We considered the parallel (FM coupling) and antiparallel (AFM coupling) spin configurations for the adjacent two Mn atoms in 2Mn_{2Mo}. We found that FM coupling is slightly more stable than AFM coupling. The spin density of Mn_{Mo} has been calculated and is shown in Figure S2 in the Supporting Information. The PDOS of 2Mn_{2Mo} suggests that the hybridization of Mn-3d, S-3p, and Mo-4d orbitals induces only localized spin-down states near the Fermi level

and are identical for FM and AFM coupling, resulting in a magnetic moment of 2 $\mu_{\rm B}$ for both couplings, Figure 5(c). Therefore, clustering of Mn_{Mo} defects with low formation energies preserves magnetic ordering.

Since the electronic structure of MoS_2 is very similar to WS_2 , we expect that all the Mn defects discussed above will show the same behavior in 2D-WS₂. Hence, here we directly consider the Mn_W-Mn_W (or $2Mn_{2W}$) clustering effect in $2D-WS_2$. The spin-polarized PDOS of 2Mn_{2W} is calculated and compared with the isolated Mn_W, which is shown in Figure 5(b, d). Unlike 2Mn_{2Mo}, the identical spin-up and spin-down states of 2Mn_{2W} indicate no magnetic ordering at the defect site, Figure 5(d). 2Mn_{2W} induces stronger structural distortion in WS₂ than in MoS₂, pulling the Mn atoms apart and delocalizing the spin-polarized states, leading to zero magnetic moment. Isolated Mn_W shows a similar behavior to Mn_{Mo} and depicts that there are more spin-up than spin-down states, signifying that Mn atoms couple with neighboring S atoms in the FM order. Isolated Mn_W induces a local magnetic moment of 1 μ_B , Figure 5(b). The spin density of Mn_{Mo} has been calculated and is shown in Figure S2 in the Supporting Information. We attribute this change in magnetic defect clustering behavior to the greater difference in atomic radius between Mn and W than Mn and Mo, which introduces larger lattice distortion at the substitution site.

We analyzed the DTLs of clustered 2Mn_{2Mo} and 2Mn_{2W} and compared them with the DTLs of isolated Mn_{Mo} and Mn_W as a function of the Fermi level ($E_{\rm F}$) in Mo-rich, W-rich, and S-rich conditions, as shown Figure 6. The E^{t} of $2Mn_{Mo}$ is 3.30 eV under Mo-rich conditions and −1.4 eV under S-rich conditions. Therefore, 2Mn_{2Mo} is more likely to form in the S-rich growing sample of 2D-MoS₂. On the other hand, isolated Mn_{Mo} is thermodynamically more stable than the 2Mn_{2Mo} clusters in the Mo-rich condition. Noticeably, 2Mn⁰_{2Mo} favors FM coupling over AFM coupling by 150 meV, Figure 6(a, b). 2Mn⁺¹_{2Mo} provides a shallow donor level in AFM coupling, and the DTL of $2Mn^{\varepsilon(+1/0)}_{2Mo}$ occurs at $E_{\text{CBM}} = 0.22 \text{ eV}$, which means that when $E_{\text{Fermi}} = E_{\text{CBM}}$, 2Mn⁰_{2Mo} is the most stable defect and the electron excitation of $2Mn_{2Mo}^{0} \rightarrow 2Mn^{+1} + e^{-}$ requires 0.22 eV, where e^{-} is a conduction electron, Figure 6(a, b). However, in the FM coupling, 2Mn_{2Mo} provides a deep donor level and the associated DTL occurs at $E_{CBM} = 0.51$ eV. Therefore, 2Mn_{2Mo} is a useful magnetic defect in AFM coupling, which can enhance the n-type conductivity of 2D-MoS2. Interestingly, when the $E_{\rm F}$ is more than 0.22 eV below the $E_{\rm CBM}$, $2{\rm Mn}^{+1}_{2{\rm Mo}}$ is thermodynamically more stable in AFM coupling than FM coupling, as shown in Figure 6(a, b). Moreover, $2Mn^{+1}_{2Mo}$ induces a local magnetic moment of 3 $\mu_{\rm B}$ in the AFM coupling. On the other hand, the isolated Mn⁰_{Mo} coupled with the nearest six S atoms is most stable in an AFM configuration, but Mn⁻¹_{Mo} prefers FM coupling. The added electron occupies the previously unoccupied defect state just above the E_F and gives a local magnetic moment of 2 μ_B . $\mathrm{Mn^{+1}}_{\mathrm{Mo}}$ exhibits nonmagnetic behavior, where the donor state just below the $E_{\rm F}$ (Figure 4(a)) transfers its electron to the conduction band and the net magnetic moment goes to zero.

As-grown 2D-MoS₂ is an n-type semiconductor, and it is found that the equilibrium $E_{\rm F}$ position is located at 0.6 eV below the CBM; this does not change significantly with the growth conditions. Therefore, we have considered $E_{\rm F}^{300~{\rm K}}$ to be the same for Mo-rich and S-rich conditions, as shown in Figure 6(a, b). At $E_{\rm F}^{300~{\rm K}}$, 2Mn_{2Mo} and Mn_{Mo} are most stable in

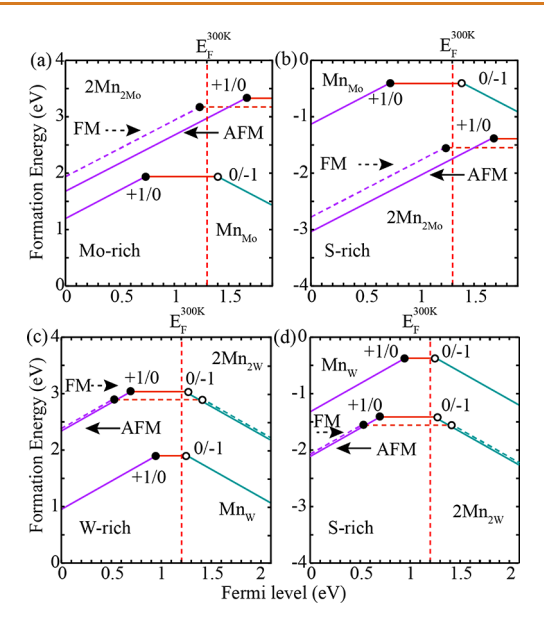


Figure 6. Comparison of an isolated Mn doping with its clustering in 2D-MoS $_2$ [(a) and (b)] and 2D-WS $_2$ [(c) and (d)]. Formation energies of an isolated Mn $_{Mo}$ and Mn–Mn clustering (2Mn $_{2Mo}$) in 2D-MoS $_2$, under the (a) Mo-rich condition and (b) S-rich condition, as a function of the Fermi level ($E_{\rm F}$). Formation energies of an isolated Mn $_{\rm W}$ and Mn–Mn clustering (2Mn $_{2\rm W}$) in 2D-WS $_2$, under the (c) W-rich condition and (d) S-rich condition, as a function of the $E_{\rm F}$. Experimentally, it is observed that the $E_{\rm F}$ position of 2D-MoS $_2$ and 2D-WS $_2$ changes very little for the Mo(W) and S-rich growth conditions at room temperature; therefore, we use the same $E_{\rm F}$ position in Mo (or W)-rich and S-rich conditions (vertical red dashed lines). The solid and dashed segments represent the antiferromagnetic and ferromagnetic configurations. The significance of these lines and circles is the same as those in Figure 3.

+1 and neutral charge states, respectively. The high $E^{\rm f}$ of $2{\rm Mn^{+1}}_{2{\rm Mo}}$ at $E_{\rm F}^{300~{\rm K}}$ in the Mo-rich condition requires high temperature to be activated and supports the intrinsic n-type conductivity of 2D-MoS₂, Figure 6(a). Fortunately, the low $E^{\rm f}$ of $2{\rm Mn^{+1}}_{2{\rm Mo}}$ at $E_{\rm F}^{300~{\rm K}}$ in the S-rich condition provides excess free electron carriers and increases the n-type conductivity of 2D-MoS₂ even at low temperatures, Figure 5(b). As Mn_{Mo} is an electrically inactive defect at the $E_{\rm F}^{300~{\rm K}}$, it does not play any role in electrical conduction in the thermodynamic equilibrium condition.

The E^{t} of Mn_{W}^{0} is 1.93 and -0.3 eV in the W-rich and S-rich condition, respectively, which suggests its high concentration in the S-rich growth condition, Figure 6(c, d). Similar to Mn_{Mo} , isolated Mn_W is found as an amphoteric defect in 2D-WS₂. The DTLs of $Mn^{\varepsilon(+1/0)}_W$ and $Mn^{\varepsilon(0/-1)}_W$ occur at 0.95 eV below the CBM and 1.25 eV above the VBM, respectively, leading to deep defect behavior, Figure 6(c, d). In Mn_W, the Mn atoms coupled with the nearest six S atoms give an AFM configuration in the neutral charge state and FM configuration in the -1 charge state. Mn^{+1}_{W} is found to be a nonmagnetic defect. The induced magnetic moment by Mn_W is 1 μ _B and 2 $\mu_{\rm B}$ in the neutral and -1 charge state, respectively. The clustered 2Mn_{2W} is more stable in AFM configuration than the FM configuration by 150 meV. The E^f of $2Mn^0_{2W}$ in AFM configuration is 3 and -1.37 eV in the W-rich and S-rich condition, resulting in its high concentration in S-rich grown samples of 2D-WS₂. Unlike 2Mn_{2Mo}, 2Mn_{2W} is found to be an amphoteric defect, and the thermodynamic properties of FM

and AFM configuration are nearly identical, as shown in Figure 6(c, d). The DTLs of $2Mn^{\epsilon(+1/0)}_{2W}$ and $2Mn^{\epsilon(0/-1)}_{2W}$ are located at 1.4 eV below the CBM and 1.22 eV above the VBM in the AFM configuration, and in the FM configuration, DTLs are located at 1.48 below the CBM and 1.27 eV above the VBM. Therefore, 2Mn_{2W} is a charge-compensating defect and cannot lead to electrical conductivity to 2D-WS₂. Moreover, $2Mn_{2W}$ provides a magnetic moment of 1 μ_B in the -1 charge state of FM coupling, but does not induce the magnetic moment in any other charge state. As-grown 2D-WS2 is an ntype semiconductor with $E_{\rm F}^{300~\rm K}$ positioned at 0.9 eV below the CBM, as shown in Figure 6(c, d). Interestingly, isolated Mn_W and cluster 2Mn_{2W} are stable in their neutral charge state at $E_{\scriptscriptstyle F}^{300~{
m K}}$. Therefore, they are electrically inactive defects in the thermodynamically equilibrium condition and will not lead to any electrical conduction in 2D-WS₂.

Doping a semiconducting material with electron and hole carriers changes the interaction between defects and, by extension, the magnetic coupling of that material. Therefore, we calculate the energy difference between FM and AFM coupling ($\Delta_{\text{FM-AFM}}$) of 2Mn_{2Mo} and 2Mn_{2W} as a function of electron and hole doping, as shown in Figure 7(a, b). Negative

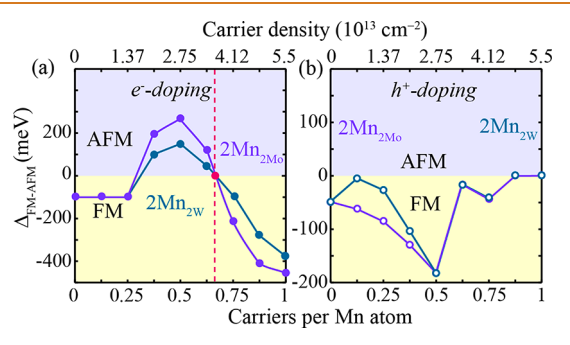


Figure 7. Energy difference between ferromagnetic (FM) and antiferromagnetic (AFM) orders as a function of (a) electron and (b) hole doping in 2D-MoS₂ and 2D-WS₂. Colors represent their respective defects. The bottom and top x-axis represent the number of doped electrons/holes per Mn atom and the corresponding carrier concentrations. The positive (violet shade) and negative (yellow shade) values of $\Delta_{\rm FM-AFM}$ indicate the AFM and FM stability, respectively. Filled and open circles represent the electron and hole carriers. Vertical magenta dashed lines indicate the phase transition of magnetic ordering from AFM to FM at a critical electron density.

values of $\Delta_{\text{FM-AFM}}$ indicate a preference for FM coupling. In the neutral system of 2Mn_{2Mo} and 2Mn_{2W}, FM coupling is more favorable than AFM coupling by $\Delta_{FM-AFM} = -150$ meV. We have previously discussed that in n-doped 2D-MoS₂ and 2D-WS₂, 2Mn_{2Mo} and 2Mn_{2W} are stable in the neutral charge state and -1 charge state, respectively (Figure 6). Here, we observe that when 2D-MoS2 and 2D-WS2 are n-doped, 2Mn_{2Mo} and 2Mn_{2W} are stable in FM coupling until the minimum value reaches 0.25e/Mn ($n_e = 1.37 \times 10^{13}$ cm⁻²); beyond that, AFM coupling is stable, as shown in Figure 7(a). AFM stability reaches its maximum value at 0.5e/Mn ($n_e =$ 2.75×10^{13} cm⁻²) and then starts decreasing until the AFM coupling is no longer stable after $n_e = 3.5 \times 10^{13} \text{ cm}^{-2}$. Therefore, there is a phase transition from AFM to FM coupling at a critical electron density $n_e^c = 3.5 \times 10^{13} \text{ cm}^{-2}$, as shown in Figure 7(a). In the p-doped 2D-MoS₂ and 2D-WS₂, $2Mn_{2Mo}$ and $2Mn_{2W}$ are stable in the +1 charge state, Figure 6.

We found that for p-doped 2D-WS₂, the difference $\Delta_{\rm FM-AFM}$ of 2Mn_{2W} increases first until $n_{\rm p}=0.68\times10^{13}~{\rm cm}^{-2}$ and then decreases monotonically until a minimum value at 0.5e/Mn ($n_{\rm p}=2.75\times10^{13}~{\rm cm}^{-2}$). The $\Delta_{\rm FM-AFM}$ of 2Mn_{2Mo} decreases monotonically until a minimum value at 0.5e/Mn ($n_{\rm p}=2.75\times10^{13}~{\rm cm}^{-2}$). After 0.5e/Mn, the $\Delta_{\rm FM-AFM}$ of both 2Mn_{2Mo} and 2Mn_{2W} increases until the FM coupling is no longer stable at 0.87e/Mn ($n_{\rm p}=4.81\times10^{13}~{\rm cm}^{-2}$) for p-doped 2D-MoS₂ and 2D-WS₂, Figure 7(b).

Next, we calculate the Curie temperature (T_c) from $\Delta_{\text{FM-AFM}}$ using the following equation, which is based on the mean-field approximation (MFA);

$$\frac{3}{2}k_{\rm B}T_{\rm c} = \Delta_{\rm FM-AFM}/n$$

where $k_{\rm B}$ is the Boltzmann constant and n=2 is the number of Mn atoms as clustered in the supercell. The calculated $T_{\rm c}$ as a function of carrier density is shown in Figure 8. At a 1.85%

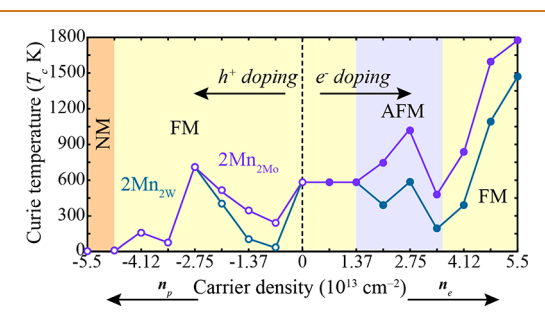


Figure 8. Variation of calculated Curie temperature of $2Mn_{2Mo}$ and $2Mn_{2W}$ clusters induced magnetism in $2D\text{-MoS}_2$ and $2D\text{-WS}_2$, as a function of doped carrier density. Negative and positive values on the *x*-axis represent the hole and electron density, respectively. Yellow, violet, and orange shades indicate the FM, AFM, and nonmagnetic (NM) regions. Colors describe their respective defects.

concentration of Mn, we calculate a Curie temperature of 580 K in the MFA. Furthermore, we estimate that $T_{\rm c}$ can reach up to 1800 and 1500 K at $1e/{\rm Mn}$ ($n_{\rm e}=5.5\times10^{13}~{\rm cm}^{-2}$) for the n-doped 2D-MoS₂ and WS₂, respectively. Moreover, for the p-doped condition, the calculated $T_{\rm c}$ is 700 K at 0.5e/Mn ($n_{\rm p}=2.75\times10^{13}~{\rm cm}^{-2}$). A recent report⁵⁷ suggests that isolated Mn_W (Mn_{Mo}) in 2D-WS₂ (2D-MoS₂) shows a huge perpendicular magnetic anisotropy of 35 meV (8 meV). However, 2Mn_{2w} and 2Mn_{2Mo} show a relatively weak MAE compared to isolated Mn_W and Mn_{Mo} in 2D-WS₂ and 2D-MoS₂, respectively. This means that although clustering of defects can preserve magnetic ordering, the easy axis may be less well determined in these clustered arrangements; in future work, we expect to investigate the effect of electrical doping on the MAE in these systems.

CONCLUSIONS

In summary, using hybrid density functional theory, we analyzed the defect thermodynamics and the magnetic properties of possible Mn defects in 2D-MoS $_2$ and 2D-WS $_2$. Most of the Mn defects are found to be deep and charge compensating. Interestingly, Mn_{Mo} and $2Mn_{Mo}$ are stable as amphoteric and negative-U defects, respectively, contradicting previous classifications as donor defects. We observe that $2Mn_{2Mo}$ and $2Mn_{2W}$ clusters are stable in FM coupling, and they are more likely to form in S-rich grown samples. Unlike

isolated Mn_{Mo}, a 2Mn_{2Mo} cluster provides a shallow donor level in AFM coupling; however, it is a deep donor defect in FM coupling. 2Mn_{2W} is found to be a deep defect, which acts as charge trap center in FM and AFM coupling. At a 1.85% concentration of Mn, we calculate the Curie temperature of 580 K in the mean-field approximation. Although $T_{\rm c}$ is overestimated in the mean-field approximation, we estimate that $T_{\rm c}$ can reach up to 1800 and 1500 K, and 700 K for the n-doped and p-doped 2D-MoS₂ and 2D-WS₂, respectively, which exceed previously calculated values for other 2D ferromagnets under the same model framework by more than 600 K. States of the coupling of the coupling

METHODS

All first-principles calculations are carried out using the projectoraugmented-wave (PAW) method as implemented in the Vienna Ab initio Simulation Package (VASP); 59,60 the exchange-correlation is treated using the Perdew-Burke-Ernzerhof (PBE) generalized gradient approximation for relaxing the atomic positions,⁵⁹ and all subsequent calculations use the Heyd-Scuseria-Ernzerhof (HSE06)^{61,62} hybrid exchange-correlation functional. An HSE06 mixing parameter $\alpha = 0.10$ and screening parameter $\mu = 0.2 \text{ Å}^{-1}$ are chosen for accurate calculations. This functional is chosen to obtain more accurate band gap values than can be achieved within the local density⁶³ and generalized gradient approximations.⁶⁴ The kinetic energy cutoff of the plane-wave basis was set to 400 eV. The structural optimization is performed until the residual forces acting on the atoms are less than 0.005 eV/Å. A dense Monkhorst–Pack b-point grid $(21 \times 21 \times 1)$ is used for geometry optimization of the unit cell of 2D-MoS₂ and 2D-WS₂. Spin polarization of the defects is considered in these defect calculations. As a previous²⁹ study suggests a lesser effect of spin-orbit coupling on the DTLs of 2D-MoS₂ and 2D-WS₂, therefore, the SOC effect is ignored in the calculations. To correct for spurious Coulombic interactions arising from periodic defect images, we have converged the formation energies as a function of supercell size. Previous studies suggest that in 2D-MoS₂ (2D-WS₂) a vacuum distance of more than 15 Å of any charged defect is sufficient to predict the isolated defect formation energies (E^{f}) within ~0.15 eV error for single charge states $(q = \pm 1)$, and we added a vacuum spacing of ~19 Å for the $6 \times 6 \times 1$ supercell and ~25 Å for the $8 \times 8 \times 1$ supercell, in the *z*-direction. ^{50,66,67} A 2 ×2 × 1 *k*-point sampling is used for all the subsequent calculations, which is done with an $8 \times 8 \times$ 1 (containing 192 atoms) in-plane supercell size. Moreover, to check the accuracy of our calculated results using the supercell approach, we compared the E^f of V_S in the -1 charge states (i.e., V_S^{-1}) in 2D-MoS₂ with the previous report.⁶⁸ The variation of the E^f of V_S^{-1} with the function of supercell size is shown in Figure S1(a) of the Supporting Information. The calculated E^f of V_S^{-1} is 3.27 eV in the Mo-rich condition for the large supercell size of $8 \times 8 \times 1$ ($L_x = L_y = L_z \approx 25 \text{ Å}$ and containing 192 atoms), which agrees well with reported values, i.e., ~3.25 eV in the Mo-rich condition. Moreover, Figure S1(b and c) shows the variation of E^f of Mn_{Mo}^{-1} and Mn_{Mo}^{+1} , respectively, with the supercells of 2D-MoS₂. We found that the $8 \times 8 \times \bar{1}$ supercell size is large enough to predict the isolated E^{f} ; therefore, it is considered for all subsequent calculations.

ASSOCIATED CONTENT

5 Supporting Information

The Supporting Information is available free of charge at https://pubs.acs.org/doi/10.1021/acsnano.2c02387.

Variation of defect formation energies of V_S and Mn_{Mo} in 2D-MoS₂, spin density of Mn_{Mo} , Mn_{W} , $2Mn_{2Mo}$, and $2Mn_{2W}$; defect transition levels of Mn_S , $2Mn_{Mo}$, Mn-top, and Mn_{Mo} in Mo-rich and S-rich conditions in 2D-MoS₂, as a function of Fermi level (PDF)

AUTHOR INFORMATION

Corresponding Author

Vivek B. Shenoy – Department of Materials Science and Engineering, University of Pennsylvania, Philadelphia, Pennsylvania 19104, United States; Email: vshenoy@seas.upenn.edu

Authors

Akash Singh — Department of Materials Science and Engineering, University of Pennsylvania, Philadelphia, Pennsylvania 19104, United States; orcid.org/0000-0001-6428-6413

Christopher C. Price – Department of Materials Science and Engineering, University of Pennsylvania, Philadelphia, Pennsylvania 19104, United States; orcid.org/0000-0002-4702-5817

Complete contact information is available at: https://pubs.acs.org/10.1021/acsnano.2c02387

Author Contributions

The manuscript was written through contributions of all authors. All authors have given approval to the final version of the manuscript.

Notes

The authors declare no competing financial interest.

ACKNOWLEDGMENTS

This work is supported by MRSEC/DMR-1720530 from the U.S. National Science Foundation.

REFERENCES

- (1) Ohno, H. Making Nonmagnetic Semiconductors Ferromagnetic. *Science* **1998**, *281*, 951–956.
- (2) Dietl, T.; Ohno, o. H.; Matsukura, a. F.; Cibert, J.; Ferrand, e. D. Zener Model Description of Ferromagnetism in Zinc-blende Magnetic Semiconductors. *Science* **2000**, 287, 1019–1022.
- (3) Ohno, H.; Chiba, a. D.; Matsukura, a. F.; Omiya, T.; Abe, E.; Dietl, T.; Ohno, Y.; Ohtani, K. Electric-field Control of Ferromagnetism. *Nature* **2000**, *408*, 944–946.
- (4) Dietl, T.; Ohno, H. Dilute Ferromagnetic Semiconductors: Physics and Spintronic Structures. *Rev. Mod. Phys.* **2014**, *86*, 187.
- (5) Li, X.; Yang, J. First-principles Design of Spintronics Materials. *Natl. Sci. Rev.* **2016**, *3*, 365–381.
- (6) Zunger, A.; Lany, S.; Raebiger, H. The Quest for Dilute Ferromagnetism in Semiconductors: Guides and Misguides by Theory. *Physics* **2010**, *3*, 53.
- (7) Dietl, T. A Ten-year Perspective on Dilute Magnetic Semiconductors and Oxides. *Nat. Mater.* **2010**, *9*, 965–974.
- (8) Coey, J.; Venkatesan, M.; Fitzgerald, C. Donor Impurity Band Exchange in Dilute Ferromagnetic Oxides. *Nat. Mater.* **2005**, *4*, 173–179.
- (9) Matsumoto, Y.; Murakami, M.; Shono, T.; Hasegawa, T.; Fukumura, T.; Kawasaki, M.; Ahmet, P.; Chikyow, T.; Koshihara, S.-y.; Koinuma, H. Room Temperature Ferromagnetism in Transparent Transition Metal-doped Titanium Dioxide. *Science* **2001**, *291*, 854–856.
- (10) Sato, K.; Bergqvist, L.; Kudrnovský, J.; Dederichs, P. H.; Eriksson, O.; Turek, I.; Sanyal, B.; Bouzerar, G.; Katayama-Yoshida, H.; Dinh, V.; Fukushima, T.; Kizaki, H.; Zeller, R. First-principles Theory of Dilute Magnetic Semiconductors. *Rev. Mod. Phys.* **2010**, *82*, 1633.
- (11) Zhang, H.; Li, Y.; Hou, J.; Tu, K.; Chen, Z. FeB₆ Monolayers: The Graphene-like Material with Hypercoordinate Transition Metal. *J. Am. Chem. Soc.* **2016**, *138*, 5644–5651.

- (12) Cheng, W.; He, J.; Yao, T.; Sun, Z.; Jiang, Y.; Liu, Q.; Jiang, S.; Hu, F.; Xie, Z.; He, B.; Yan, W.; Wei, S. Half-unit-cell α -Fe₂O₃ Semiconductor Nanosheets with Intrinsic and Robust Ferromagnetism. *J. Am. Chem. Soc.* **2014**, *136*, 10393–10398.
- (13) Huang, B.; Clark, G.; Navarro-Moratalla, E.; Klein, D. R.; Cheng, R.; Seyler, K. L.; Zhong, D.; Schmidgall, E.; McGuire, M. A.; Cobden, D. H.; Yao, W.; Xiao, D.; Jarillo-Herrero, P.; Xu, X. Layer-dependent Ferromagnetism in a Van der Waals Crystal Down to the Monolayer Limit. *Nature* **2017**, *546*, 270–273.
- (14) Gong, C.; Li, L.; Li, Z.; Ji, H.; Stern, A.; Xia, Y.; Cao, T.; Bao, W.; Wang, C.; Wang, Y.; Qiu, Z. Q.; Cava, R. J.; Louie, S. G.; Xia, J.; Zhang, X. Discovery of Intrinsic Ferromagnetism in Two-dimensional Van der Waals Crystals. *Nature* **2017**, *546*, 265–269.
- (15) Zhang, X.; Zhang, J.; Zhao, J.; Pan, B.; Kong, M.; Chen, J.; Xie, Y. Half-metallic Ferromagnetism in Synthetic Co₉Se₈ Nanosheets with Atomic Thickness. J. Am. Chem. Soc. **2012**, 134, 11908–11911.
- (16) Tan, C.; Cao, X.; Wu, X.-J.; He, Q.; Yang, J.; Zhang, X.; Chen, J.; Zhao, W.; Han, S.; Nam, G.-H.; Sindoro, M.; Zhang, H. Recent Advances in Ultrathin Two-dimensional Nanomaterials. *Chem. Rev.* **2017**, *117*, 6225–6331.
- (17) Miao, N.; Xu, B.; Bristowe, N. C.; Zhou, J.; Sun, Z. Tunable Magnetism and Extraordinary Sunlight Absorbance in Indium Triphosphide Monolayer. *J. Am. Chem. Soc.* **2017**, *139*, 11125–11131.
- (18) Zhang, Z.; Wu, X.; Guo, W.; Zeng, X. C. Carrier-tunable Magnetic Ordering in Vanadium- Naphthalene Sandwich Nanowires. *J. Am. Chem. Soc.* **2010**, *132*, 10215–10217.
- (19) Duan, X.; Wang, C.; Pan, A.; Yu, R.; Duan, X. Two-dimensional Transition Metal Dichalcogenides as Atomically Thin Semiconductors: Opportunities and Challenges. *Chem. Soc. Rev.* **2015**, *44*, 8859–8876.
- (20) Yin, Z.; Li, H.; Li, H.; Jiang, L.; Shi, Y.; Sun, Y.; Lu, G.; Zhang, Q.; Chen, X.; Zhang, H. Single-layer MoS₂ Phototransistors. *ACS Nano* **2012**, *6*, 74–80.
- (21) Ovchinnikov, D.; Allain, A.; Huang, Y.-S.; Dumcenco, D.; Kis, A. Electrical Transport Properties of Single-layer WS₂. ACS Nano **2014**, 8, 8174–8181.
- (22) Mak, K. F.; Lee, C.; Hone, J.; Shan, J.; Heinz, T. F. Atomically Thin MoS_2 : A New Direct-Gap Semiconductor. *Phys. Rev. Lett.* **2010**, 105, 136805.
- (23) Wang, Q. H.; Kalantar-Zadeh, K.; Kis, A.; Coleman, J. N.; Strano, M. S. Electronics and Optoelectronics of Two-dimensional Transition Metal Dichalcogenides. *Nat. Nanotechnol.* **2012**, *7*, 699–712.
- (24) Radisavljevic, B.; Radenovic, A.; Brivio, J.; Giacometti, V.; Kis, A. Single-layer MoS₂ Transistors. *Nat. Nanotechnol.* **2011**, *6*, 147–150.
- (25) Chhowalla, M.; Shin, H. S.; Eda, G.; Li, L. J.; Loh, K. P.; Zhang, H. The Chemistry of Two-Dimensional Layered Transition Metal Dichalcogenide Nanosheets. *Nat. Chem.* **2013**, *5*, 263–275.
- (26) Butler, S. Z.; Hollen, S. M.; Cao, L.; Cui, Y.; Gupta, J. A.; Gutiérrez, H. R.; Heinz, T. F.; Hong, S. S.; Huang, J.; Ismach, A. F.; Johnston-Halperin, E.; Kuno, M.; Plashnitsa, V. V.; Robinson, R. D.; Ruoff, R. S.; Salahuddin, S.; Shan, J.; Shi, L.; Spencer, M. G.; Terrones, M.; et al. Progress, Challenges, and Opportunities in Two-dimensional Materials Beyond Graphene. *ACS Nano* **2013**, *7*, 2898–2926.
- (27) Ramakrishna Matte, H.; Gomathi, A.; Manna, A. K.; Late, D. J.; Datta, R.; Pati, S. K.; Rao, C. MoS₂ and WS₂ Analogues of Graphene. *Angew. Chem., Int. Ed.* **2010**, 49, 4059–4062.
- (28) Gutiérrez, H. R.; Perea-López, N.; Elias, A. L.; Berkdemir, A.; Wang, B.; Lv, R.; López-Urías, F.; Crespi, V. H.; Terrones, H.; Terrones, M. Extraordinary Room-temperature Photoluminescence in Triangular WS₂ Monolayers. *Nano Lett.* **2013**, *13*, 3447–3454.
- (29) Singh, A.; Manjanath, A.; Singh, A. K. Engineering Defect Transition-Levels Through the Van der Waals Heterostructure. *J. Phys. Chem. C* 2018, 122, 24475–24480.
- (30) Singh, A.; Singh, A. K. Origin of n-type Conductivity of Monolayer MoS₂. *Phys. Rev. B* **2019**, *99*, 121201.

- (31) Manzeli, S.; Ovchinnikov, D.; Pasquier, D.; Yazyev, O. V.; Kis, A. 2D Transition Metal Dichalcogenides. *Nat. Rev. Mater.* **2017**, *2*, 1–15.
- (32) Choi, W.; Choudhary, N.; Han, G. H.; Park, J.; Akinwande, D.; Lee, Y. H. Recent Development of Two-dimensional Transition Metal Dichalcogenides and their Applications. *Mater. Today* **2017**, *20*, 116–130.
- (33) Wen, Y.-N.; Xia, M.-G.; Zhang, S.-L. Structural and Magnetic Properties of MoS₂ Monolayer Zigzag Nanoribbon Doped by Ti, V, Cr, and Mn. *Phys. Lett. A* **2018**, 382, 2354–2360.
- (34) Wang, J.; Sun, F.; Yang, S.; Li, Y.; Zhao, C.; Xu, M.; Zhang, Y.; Zeng, H. Robust Ferromagnetism in Mn-doped MoS₂ Nanostructures. *Appl. Phys. Lett.* **2016**, *109*, 092401.
- (35) Cai, L.; He, J.; Liu, Q.; Yao, T.; Chen, L.; Yan, W.; Hu, F.; Jiang, Y.; Zhao, Y.; Hu, T.; Sun, Z.; Wei, S. Vacancy-induced Ferromagnetism of MoS₂ Nanosheets. *J. Am. Chem. Soc.* **2015**, *137*, 2622–2627.
- (36) Yun, W. S.; Lee, J. Strain-induced Magnetism in Single-layer MoS₂: Origin and Manipulation. *J. Phys. Chem. C* **2015**, *119*, 2822–2827.
- (37) Vojvodic, A.; Hinnemann, B.; Nørskov, J. K. Magnetic Edge States in MoS₂ Characterized Using Density Functional Theory. *Phys. Rev. B* **2009**, *80*, 125416.
- (38) Li, Y.; Zhou, Z.; Zhang, S.; Chen, Z. MoS₂ Nanoribbons: High Stability and Unusual Electronic and Magnetic Properties. *J. Am. Chem. Soc.* **2008**, *130*, 16739–16744.
- (39) Mishra, R.; Zhou, W.; Pennycook, S. J.; Pantelides, S. T.; Idrobo, J.-C. Long-range Ferromagnetic Ordering in Manganese Doped Two-dimensional Dichalcogenides. *Phys. Rev. B* **2013**, *88*, 144409.
- (40) Cheng, Y.; Zhu, Z.; Mi, W.; Guo, Z.; Schwingenschlögl, U. Prediction of Two Dimensional Diluted Magnetic Semiconductors: Doped Monolayer MoS₂ Systems. *Phys. Rev. B* **2013**, *87*, 100401.
- (41) Ramasubramaniam, A.; Naveh, D. Mn-doped Monolayer MoS₂: An Atomically Thin Dilute Magnetic Semiconductor. *Phys. Rev. B* **2013**, *87*, 195201.
- (42) Zhang, K.; Feng, S.; Wang, J.; Azcatl, A.; Lu, N.; Addou, R.; Wang, N.; Zhou, C.; Ler ach, J.; Bojan, V.; Kim, M. J.; Chen, L.; Wallace, R. M.; Terrones, M.; Zhu, J.; Robinson, J. A. Manganese Doping of Monolayer MoS₂: The Substrate is Critical. *Nano Lett.* **2015**, *15*, 6586–6591.
- (43) Lei, Y.; Butler, D.; Lucking, M. C.; Zhang, F.; Xia, T.; Fujisawa, K.; Granzier-Nakajima, T.; Cruz-Silva, R.; Endo, M.; Terrones, H.; Terrones, M.; Ebrahimi, A. Single-atom Doping of MoS₂ with Manganese Enables Ultrasensitive Detection of Dopamine: Experimental and Computational Approach. *Sci. Adv.* **2020**, *6*, No. eabc4250.
- (44) Dev, P.; Xue, Y.; Zhang, P. Defect-induced Intrinsic Magnetism in Wide-gap III Nitrides. *Phys. Rev. Lett.* **2008**, *100*, 117204.
- (45) Raebiger, H.; Lany, S.; Zunger, A. Control of Ferromagnetism via Electron Doping in In₂O₃:Cr. *Phys. Rev. Lett.* **2008**, *101*, 027203.
- (46) Wu, H.; Stroppa, A.; Sakong, S.; Picozzi, S.; Scheffler, M.; Kratzer, P. Magnetism in C-or N-doped MgO and ZnO: A Density-Functional Study of Impurity Pairs. *Phys. Rev. Lett.* **2010**, *105*, 267203.
- (47) Van de Walle, C. G.; Neugebauer, J. First Principles Calculations for Defects and Impurities: Applications to III-Nitrides. *J. Appl. Phys.* **2004**, *95*, 3851–3879.
- (48) Janotti, A.; Van de Walle, C. G. Fundamentals of Zinc Oxide as a Semiconductor. *Rep. Prog. Phys.* **2009**, *72*, 126501.
- (49) Freysoldt, C.; Grabowski, B.; Hickel, T.; Neugebauer, J.; Kresse, G.; Janotti, A.; Van de Walle, C. G. First-principles Calculations for Point Defects in Solids. *Rev. Mod. Phys.* **2014**, *86*, 253.
- (50) Komsa, H.-P.; Krasheninnikov, A. V. Native Defects in Bulk and Monolayer MoS₂ from First Principles. *Phys. Rev. B* **2015**, *91*, 125304
- (51) Singh, A.; Singh, A. K. Atypical Behavior of Intrinsic Defects and Promising Dopants in Two-dimensional WS₂. *Phys. Rev. Mater.* **2021**, *5*, 084001.

- (52) Lee, C.; Yan, H.; Brus, L. E.; Heinz, T. F.; Hone, J.; Ryu, S. Anomalous Lattice Vibrations of Single-and Few-layer MoS₂. ACS Nano **2010**, 4, 2695–2700.
- (53) Elias, A. L.; Perea-López, N.; Castro-Beltrán, A.; Berkdemir, A.; Lv, R.; Feng, S.; Long, A. D.; Hayashi, T.; Kim, Y. A.; Endo, M.; Gutiérrez, H. R.; Pradhan, N. R.; Balicas, L.; Mallouk, T. E.; López-Urías, F.; Terrones, H.; Terrones, M. Controlled Synthesis And Transfer of Large-area WS₂ Sheets: From Single Layer to Few Layers. *ACS Nano* **2013**, *7*, 5235–5242.
- (54) Fleischauer, P. D.; Lince, J. R.; Bertrand, P.; Bauer, R. Electronic Structure And lubrication Properties of Molybdenum Disulfide: A Qualitative Molecular Orbital Approach. *Langmuir* **1989**, *5*, 1009–1015.
- (55) Pasquier, D.; Yazyev, O. V. Crystal Field, Ligand Field, and Interorbital Effects in Two-dimensional Transition Metal Dichalcogenides Across the Periodic Table. 2D Mater. 2019, 6, 025015.
- (56) Sotthewes, K.; Van Bremen, R.; Dollekamp, E.; Boulogne, T.; Nowakowski, K.; Kas, D.; Zandvliet, H. J.; Bampoulis, P. Universal Fermi-level Pinning in Transition-metal Dichalcogenides. *J. Phys. Chem. C* **2019**, *123*, 5411–5420.
- (57) Smiri, A.; Jaziri, S.; Lounis, S.; Gerber, I. C. DFT+U Investigation of Magnetocrystalline Anisotropy of Mn-Doped Transition-metal Dichalcogenide Monolayers. *Phys. Rev. Mater.* **2021**, *5*, 054001.
- (58) Fang, Y.; Wu, S.; Zhu, Z.-Z.; Guo, G.-Y. Large Magneto-optical Effects and Magnetic Anisotropy Energy in Two-dimensional Cr₂Ge₂Te₆. *Phys. Rev. B* **2018**, *98*, 125416.
- (59) Perdew, J. P.; Burke, K.; Ernzerhof, M. Generalized Gradient Approximation Made Simple. *Phys. Rev. Lett.* **1996**, 77, 3865.
- (60) Monkhorst, H. J.; Pack, J. D. Special Points for Brillouin-zone Integrations. *Phys. Rev. B* **1976**, *13*, 5188.
- (61) Heyd, J.; Scuseria, G. E.; Ernzerhof, M. Hybrid Functionals Based on A Screened Coulomb Potential. *J. Chem. Phys.* **2003**, *118*, 8207–8215.
- (62) Krukau, A. V.; Vydrov, O. A.; Izmaylov, A. F.; Scuseria, G. E. Influence of the Exchange Screening Parameter on the Performance of Screened Hybrid Functionals. *J. Chem. Phys.* **2006**, *125*, 224106.
- (63) Kohn, W.; Sham, L. J. Self-consistent Equations Including Exchange and Correlation Effects. *Phys. Rev.* **1965**, *140*, A1133.
- (64) Kresse, G.; Furthmüller, J. Efficiency of abinitio Total Energy Calculations for Metals and Semiconductors Using a Plane-Wave Basis Set. *Comput. Mater. Sci.* **1996**, *6*, 15–50.
- (65) Fuchs, M.; Scheffler, M. Ab initio Pseudopotentials for Electronic Structure Calculations of Poly-atomic Systems Using Density-Functional Theory. *Comput. Phys. Commun.* **1999**, *119*, 67–98.
- (66) Singh, A.; Dey, M.; Singh, A. K. Origin of Layer-Dependent Electrical Conductivity of Transition Metal Dichalcogenides. *Phys. Rev. B* **2022**, *105*, 165430.
- (67) Noh, J.-Y.; Kim, H.; Kim, Y.-S. Stability and Electronic Structures of Native Defects in Single-layer MoS₂. *Phys. Rev. B* **2014**, 89, 205417.
- (68) Tan, A. M. Z.; Freysoldt, C.; Hennig, R. G. Stability of Charged Sulfur Vacancies in 2D and Bulk MoS₂ from Plane-wave Density Functional Theory with Electrostatic Corrections. *Phys. Rev. Mater.* **2020**, *4*, 064004.